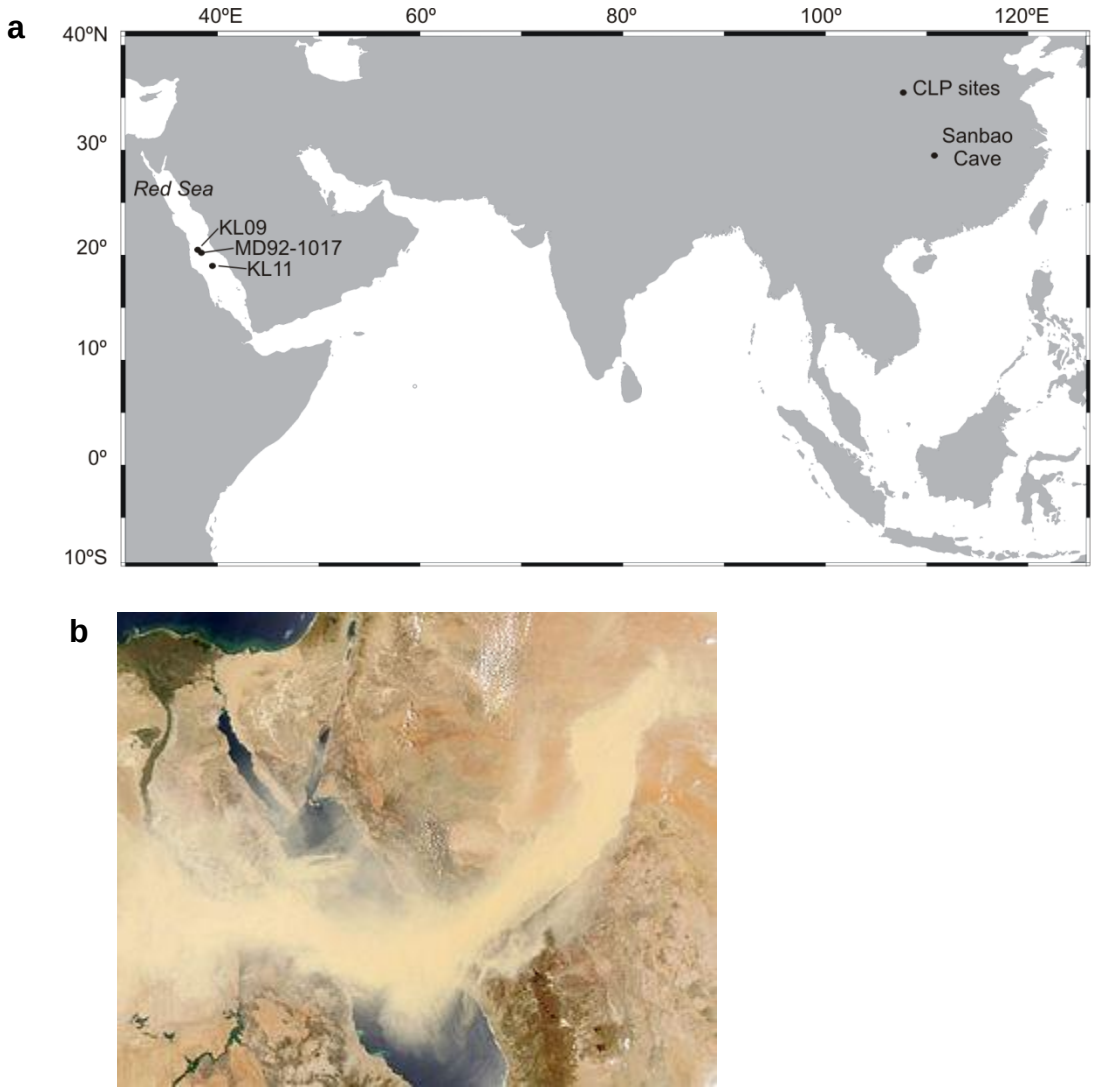

Supplementary Figure 1 Map of sites and regions discussed in this study. **a**, Location of Red Sea cores (KL09, MD92-1017, and KL11), Sanbao Cave, and the Chinese Loess Plateau (CLP) grain-size records. **b**, Satellite image of an Arabian dust storm deflected over the Red Sea. Source: http://earthobservatory.nasa.gov/IOTD/view.php?id=5500

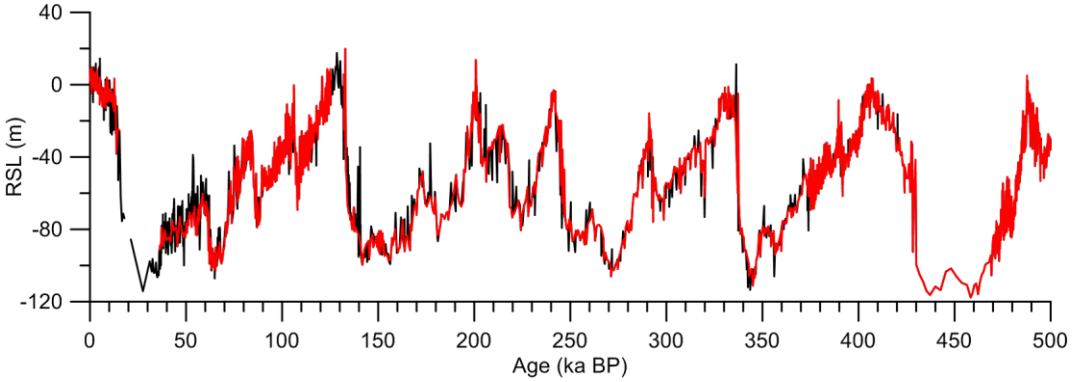

Supplementary Figure 2 Red Sea relative sea-level (RSL) records. RSL records[2]derived from KL09 data only (red; n = 1404) and from KL09, KL11 and MD92-1017 data (black; n = 1938).

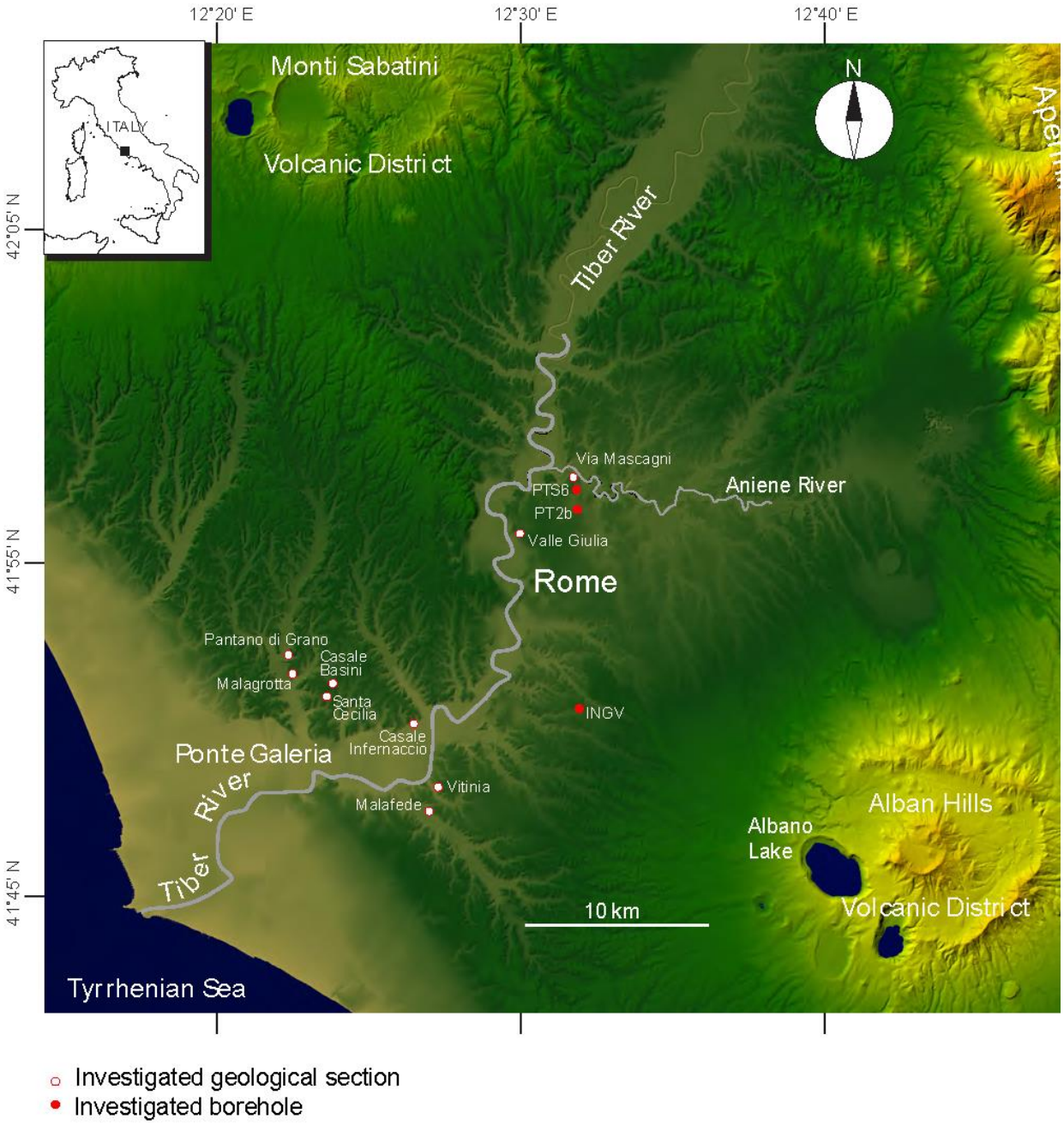

Supplementary Figure 3 Map of area around Rome, Italy, with locations of palaeomagnetic investigations and $^{40}Ar/^{39}Ar$-dated tephra used in the Palaeo-Tiber River chronostratigraphy.

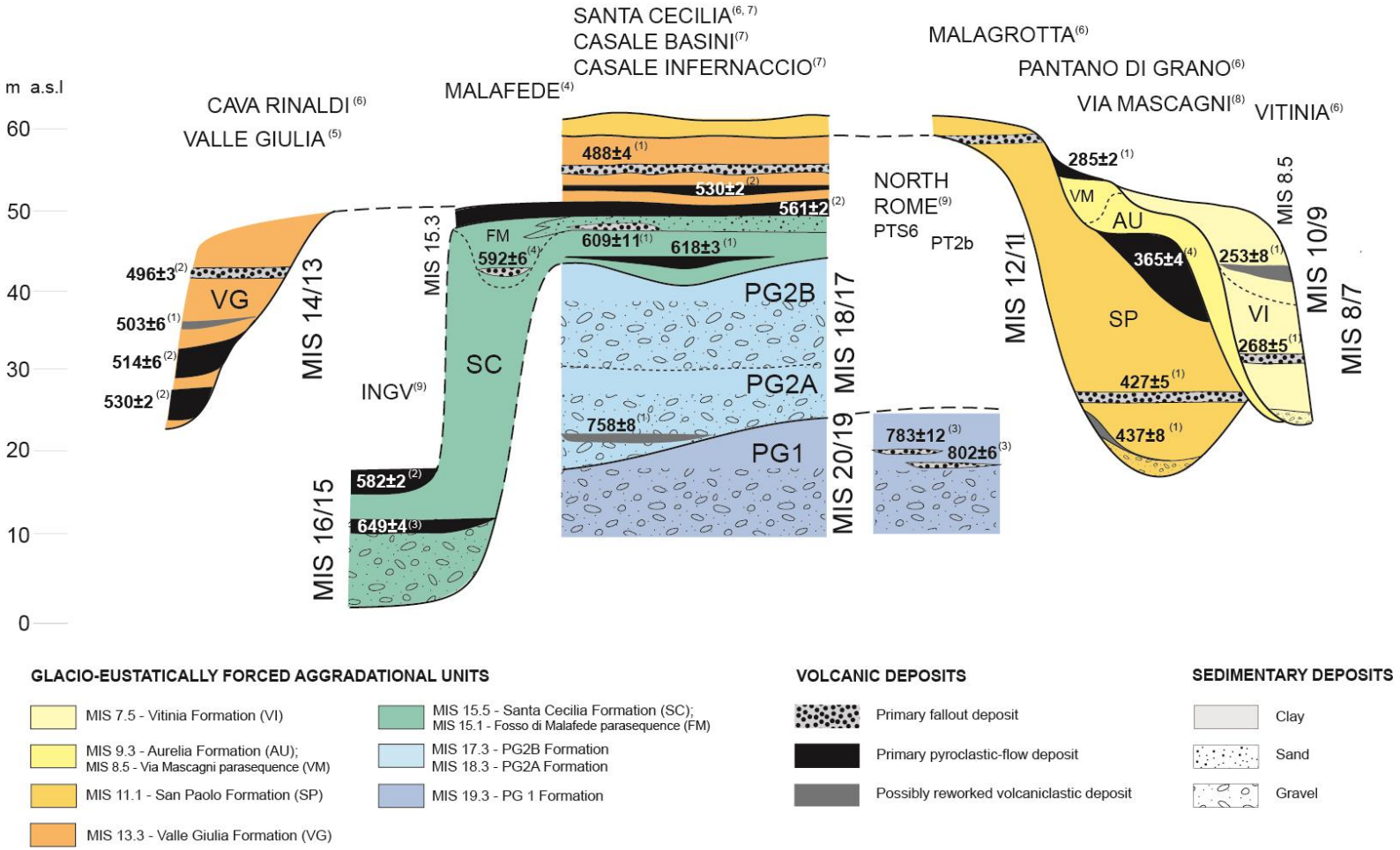

Supplementary Figure 4 Schematic geological section (not to scale) of lithostratigraphic features of aggradational Palaeo-Tiber River deposits, and the positions of dated volcanic ash layers used to constrain the timing of sea-level rise. See Fig. S8 for locations of the sections and boreholes. 'MIS' = marine isotope stage; 'm a.s.l.' = metres above sea level. $^{40}Ar/^{39}Ar$ ages in kyr (±2σ) are from: (1) ref. 19, (2) ref. 29, (3) ref. 16, (4) ref. 30. Stratigraphic section details are from: (6) ref. 31, (7) ref. 32, (8) ref. 33, (9) ref. 34, and (10) ref. 16.

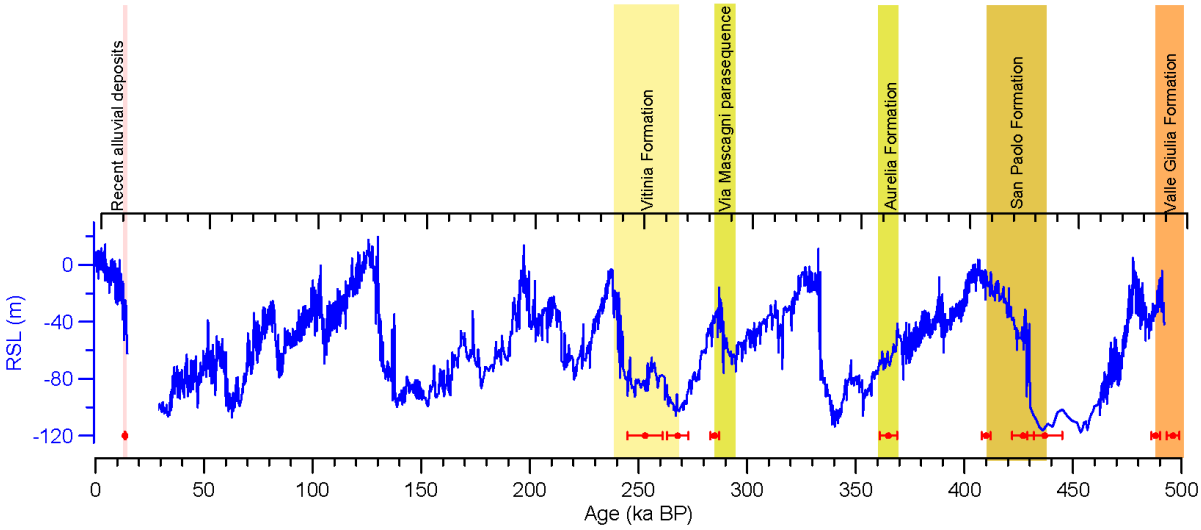

Supplementary Figure 5 $^{40}Ar/^{39}Ar$ datings (red symbols with 2σ error bars; Supplementary Table 3) from sea-level-forced depositional sequences from the Palaeo-Tiber River, compared to Red Sea RSL variations (blue). Coloured boxes (see Supplementary Fig. 4 for colour legends) schematically highlight how aggradational deposits correspond to sea-level variations.

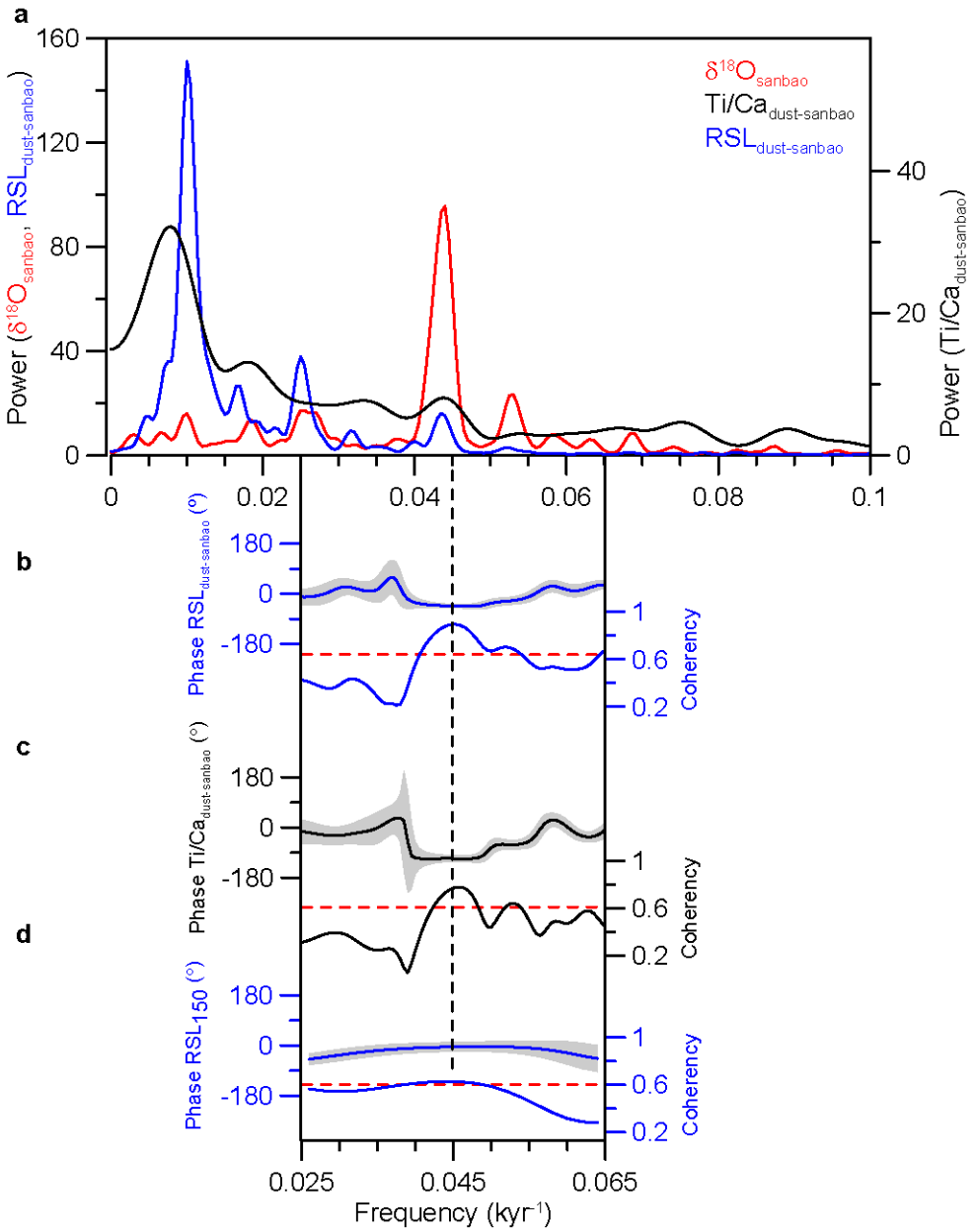

Supplementary Figure 6 a, Spectral analyses of $\delta^{18}O_{sanbao}$ (red), KL09 $Ti/Ca_{dust\text{-}sanbao}$ (black) and $RSL_{dust\text{-}sanbao}$ (blue) after the dust-$\delta^{18}O_{sanbao}$ correlation. All records have spectral peaks at a frequency of 0.042-0.045 kyr^{-1} (equivalent periodicity = 22.2-23.8kyr). **b-d**, Phase relationships between $\delta^{18}O_{sanbao}$ and $RSL_{dust\text{-}sanbao}$, $Ti/Ca_{dust\text{-}sanbao}$, and RSL_{150}, respectively. Positive phases correspond to changes in $\delta^{18}O_{sanbao}$ leading changes in the Red Sea records, and vice versa. Phase relationships are valid at significant (2σ) coherencies (dashed red lines).

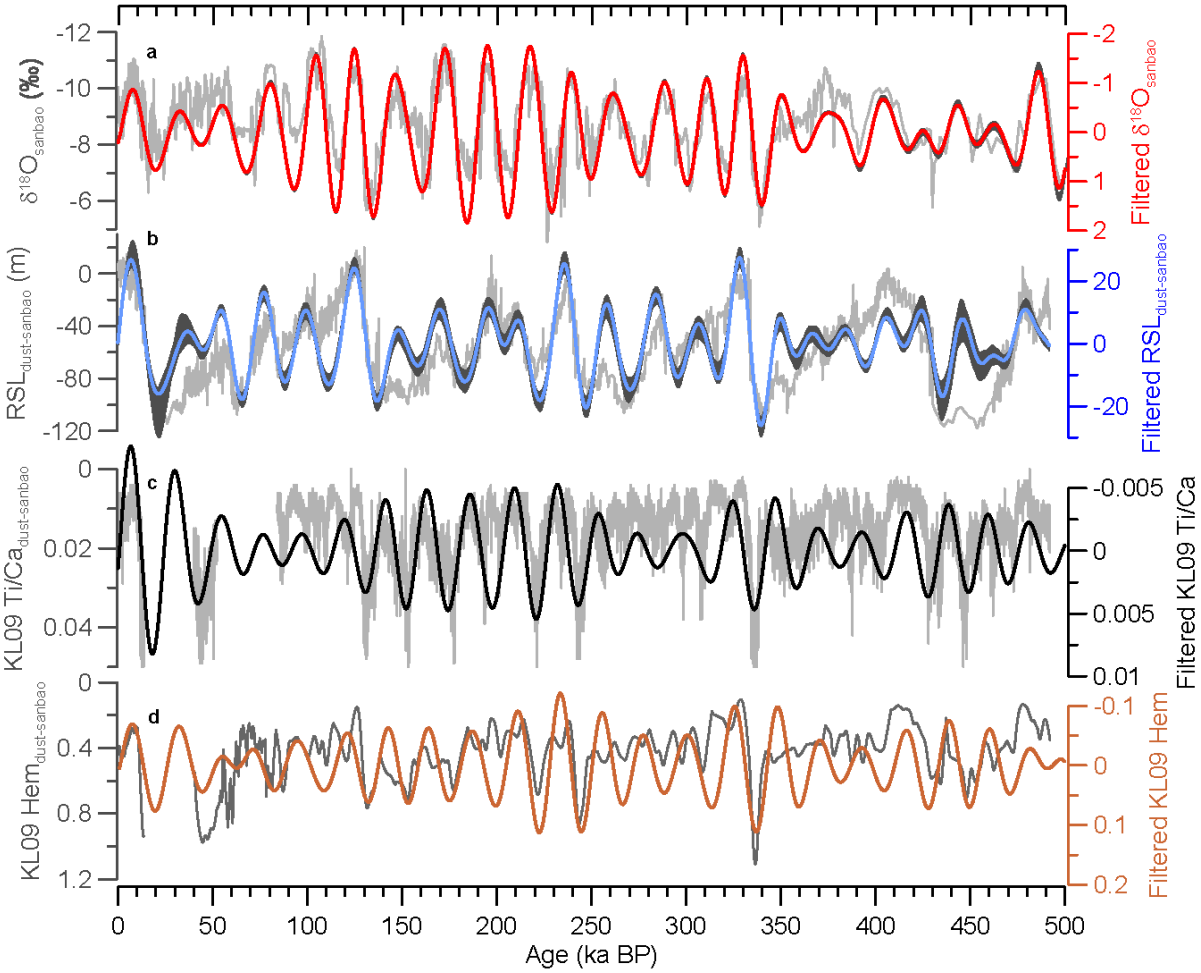

Supplementary Figure 7 22-kyr band-pass filtered records of: **a**, $\delta^{18}O_{sanbao}$ (red), **b**, $RSL_{dust\text{-}sanbao}$ (blue), **c**, KL09 Ti/Ca $_{dust\text{-}sanbao}$ (black) and **d**, KL09 Hem $_{dust\text{-}sanbao}$ (brown), superimposed on the respective (unfiltered) time-series (grey). For **a** and **b**, the results of all 1000 Monte-Carlo simulations are also plotted (dark grey envelopes). Note that the filtered $\delta^{18}O_{sanbao}$ record obscures most of the results of the Monte-Carlo simulations in **a**.

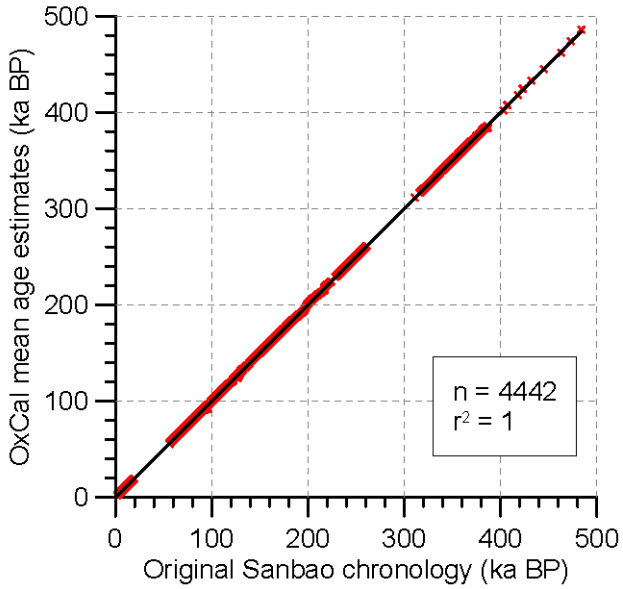

Supplementary Figure 8 Comparison of the original Sanbao Cave chronology[7,14,15], based on U/Th datings and linearly interpolated ages, with OxCal-modelled age estimates.

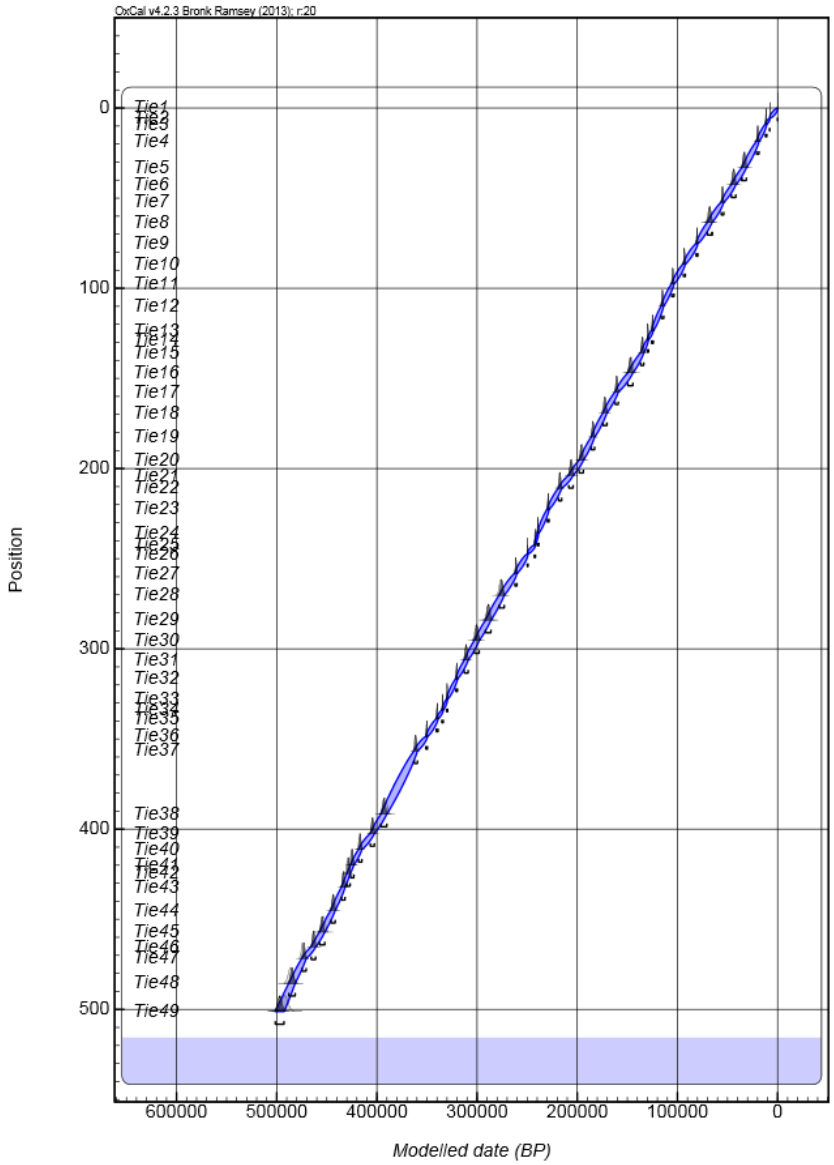

Supplementary Figure 9 Bayesian model output for all correlation tie-points. Interpolated chronological uncertainties for all RSL datapoints are derived from the 95% highest probability density (HPD) range (blue envelopes).

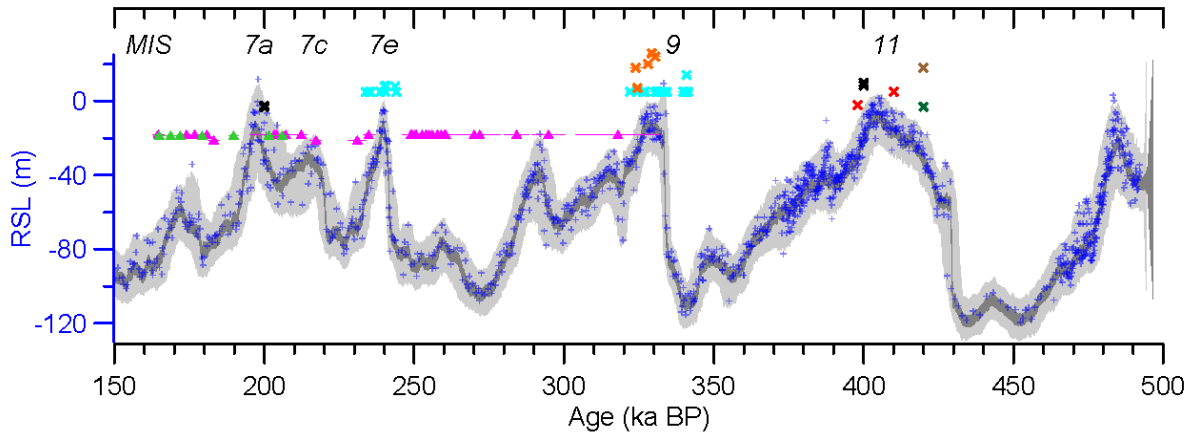

Supplementary Figure 10 Comparison of our new probabilistic RSL record [95% probability intervals of the RSL dataset (light grey) and probability maximum (dark grey)] with coral and speleothem sea-level information for sea-level highstands prior to the last interglacial (for the last interglacial period, see ref. 1). Coral sea-level data (crosses) are in black[35], cyan[36], orange[37] (data in ref. 36), red[38], brown[39], and green[40]. Speleothem data (triangles) delimit 'ceilings' to maximum sea levels (green[41]; pink[42]). Error bars are indicated if uncertainty data are available. Marine isotope stages (MIS) are also indicated.

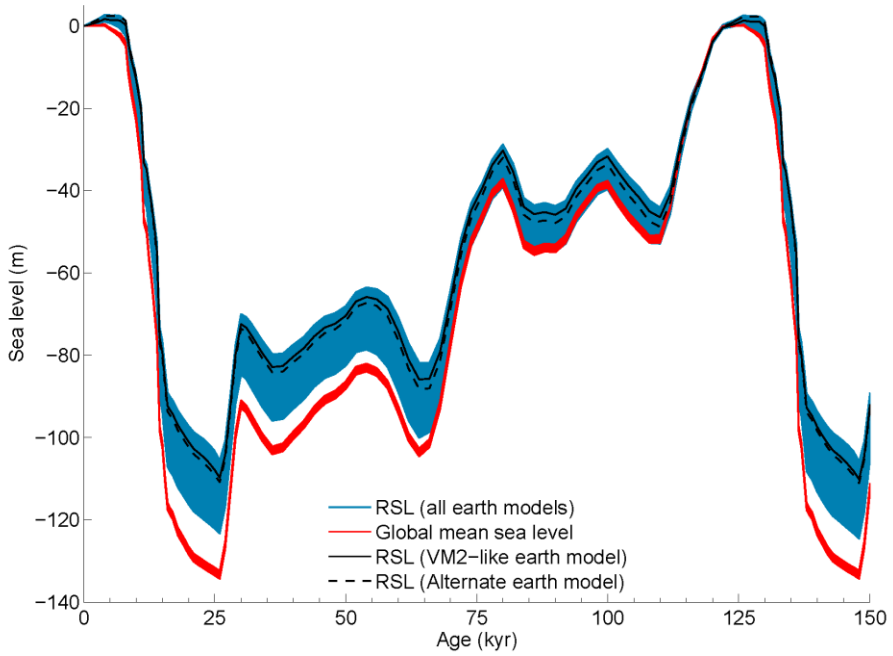

Supplementary Figure 11 ICE-5G modelled output for relative sea level (RSL) at Hanish Sill (blue) and global mean (eustatic) sea level (red). The RSL output from two Earth models is highlighted, based on a lithospheric thickness and upper and lower mantle viscosity of 96 km, 5 x 10^{20} Pa s, and 2.5 x 10^{21} Pa s (solid black line) and 71 km, 2 x 10^{20} Pa s, and 1 x 10^{22} Pa s (dashed black line), respectively.

a

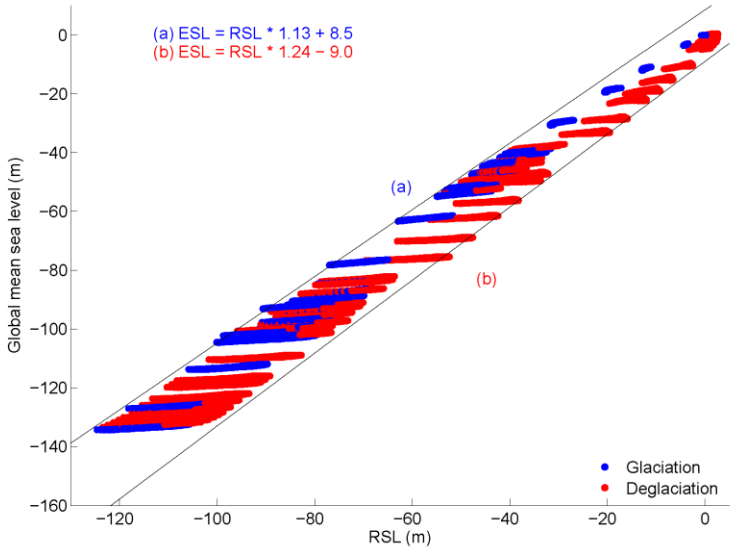

b

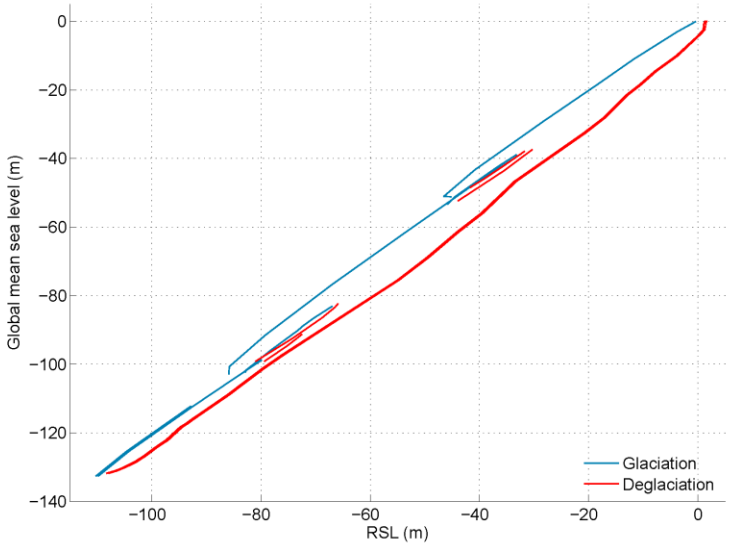

Supplementary Figure 12 ICE-5G modelled output for relative sea level (RSL) at Hanish Sill and global mean (eustatic) sea level for glaciations (blue) and deglaciations (red). **a**, Individual model runs for 495 Earth parameterisations, with linear approximations of the most extreme glaciation and deglaciation values (black lines). Equations (a) and (b) are used to convert RSL into an ESL range for calculating 'glaciation state' (see 'Maximum rates of sea-level rise' in the main text). **b**, Output for the VM2-like Earth model only.

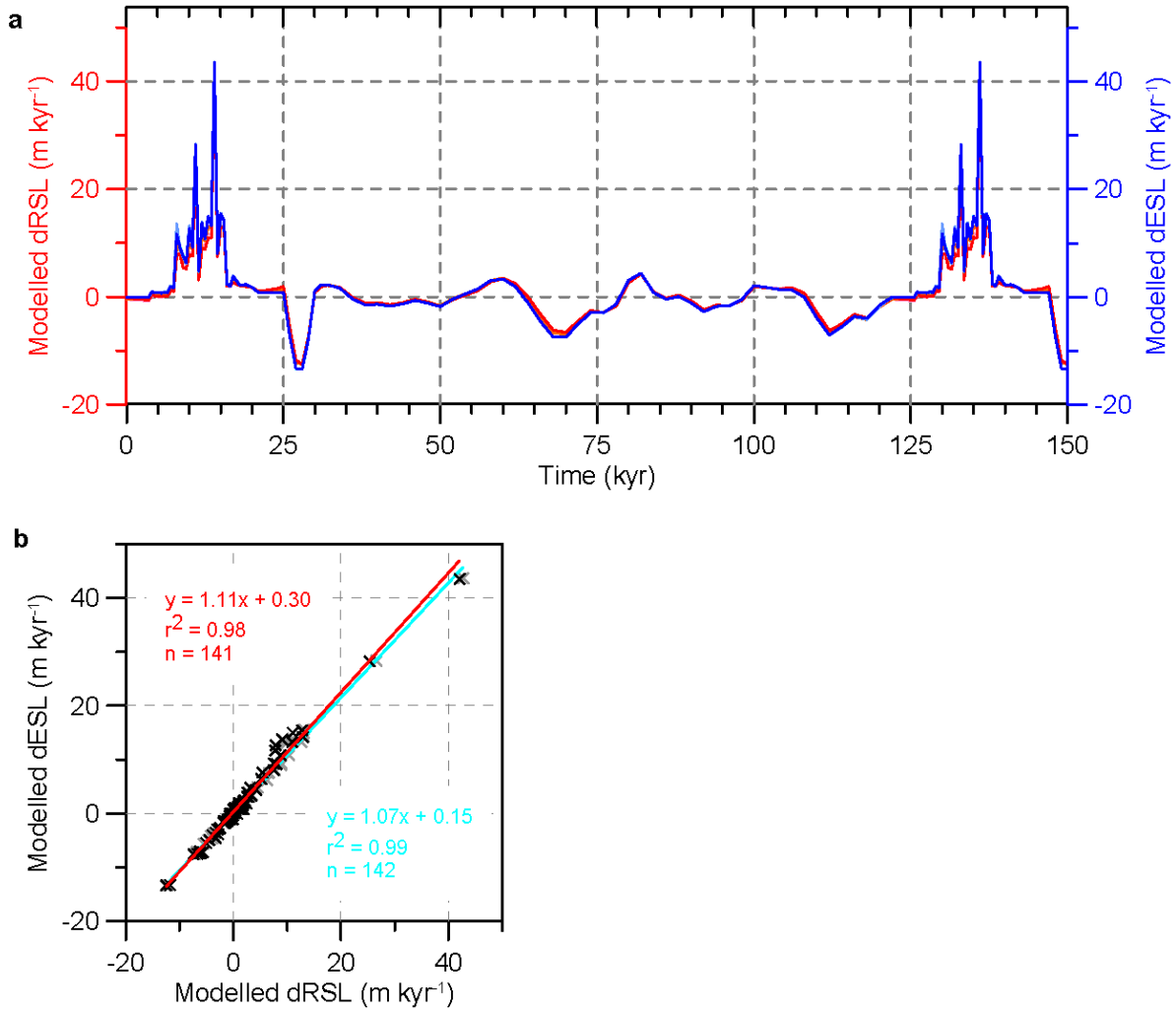

Supplementary Figure 13 a, Modelled RSL_{HS} and ESL change rates ($dRSL_{HS}$, red; dESL, blue) for the VM2-like Earth model. **b**, Linear regression between $dRSL_{HS}$ and dESL for the VM2-like Earth model (black crosses, red line) and for an alternative Earth model (grey crosses, cyan line).

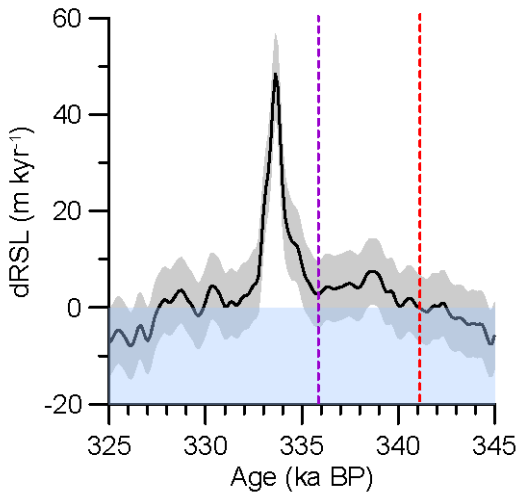

Supplementary Figure 14 Detail of sea-level rise rates (dRSL; black) and their 95% probability interval (grey shading) over a 'deglaciation event' (dRSL>0; onset denoted by red dashed line), within which a 'deglaciation pulse' is also observed (onset denoted by purple dashed line).

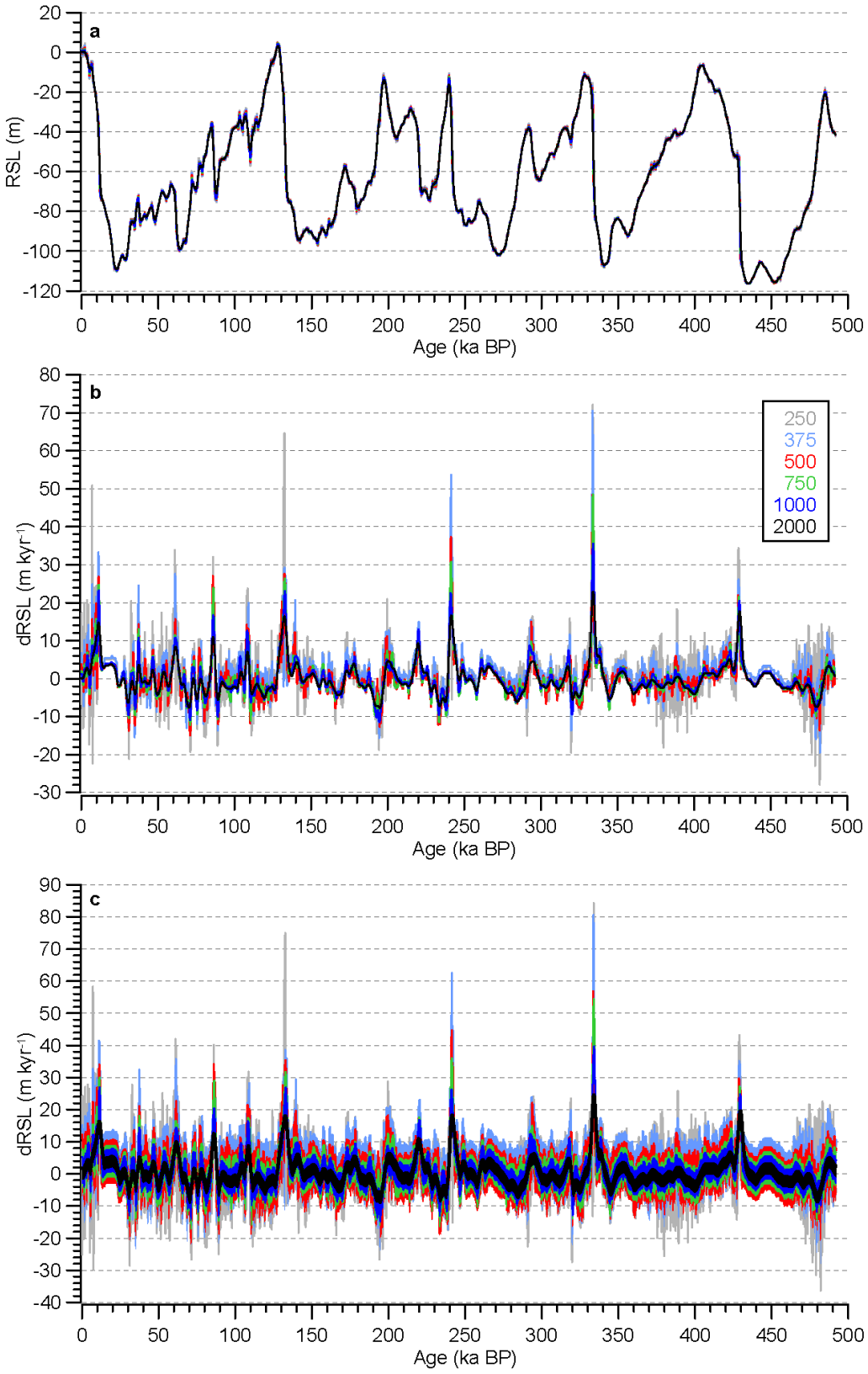

Supplementary Figure 15 The effect of RSL smoothings (250, 375, 500, 750, 1000 and 2000 year) (**a**) on 'Maximum probability' sea-level change rates (dRSL) (**b**) and the 95% probability interval of the probability maximum (**c**) (see ref. 1 for method).

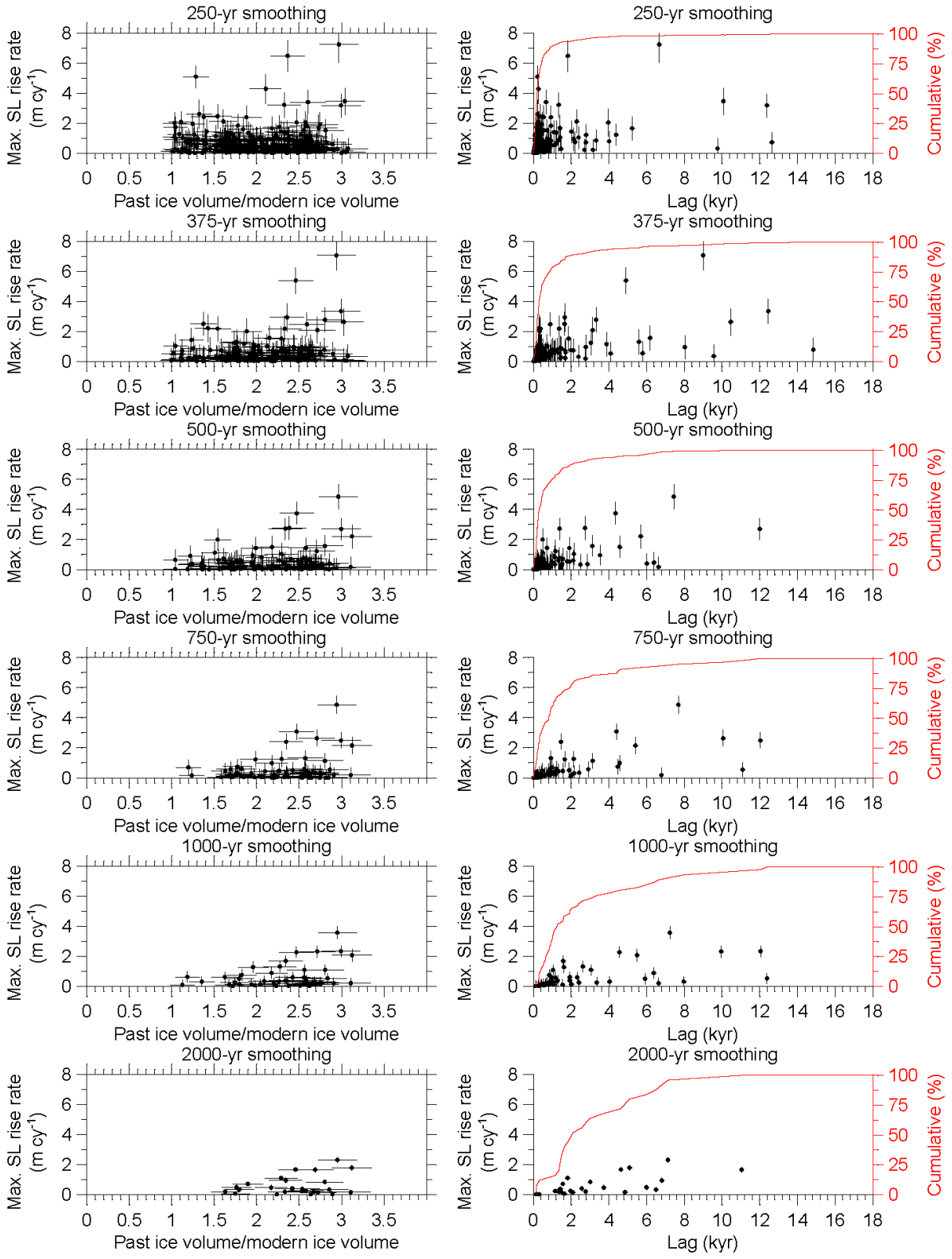

Supplementary Figure 16 Comparison of the effects of different smoothings on our analyses of deglaciation 'events'. Maximum sea-level rise rates are plotted against: (**left**) relative ice volume at the start of a deglaciation event, and (**right**) lag between the onset of deglaciation events and peak sea-level rise rates. The cumulative distribution (red line) of the number of deglaciation events as a function of lag is also shown (**right**).

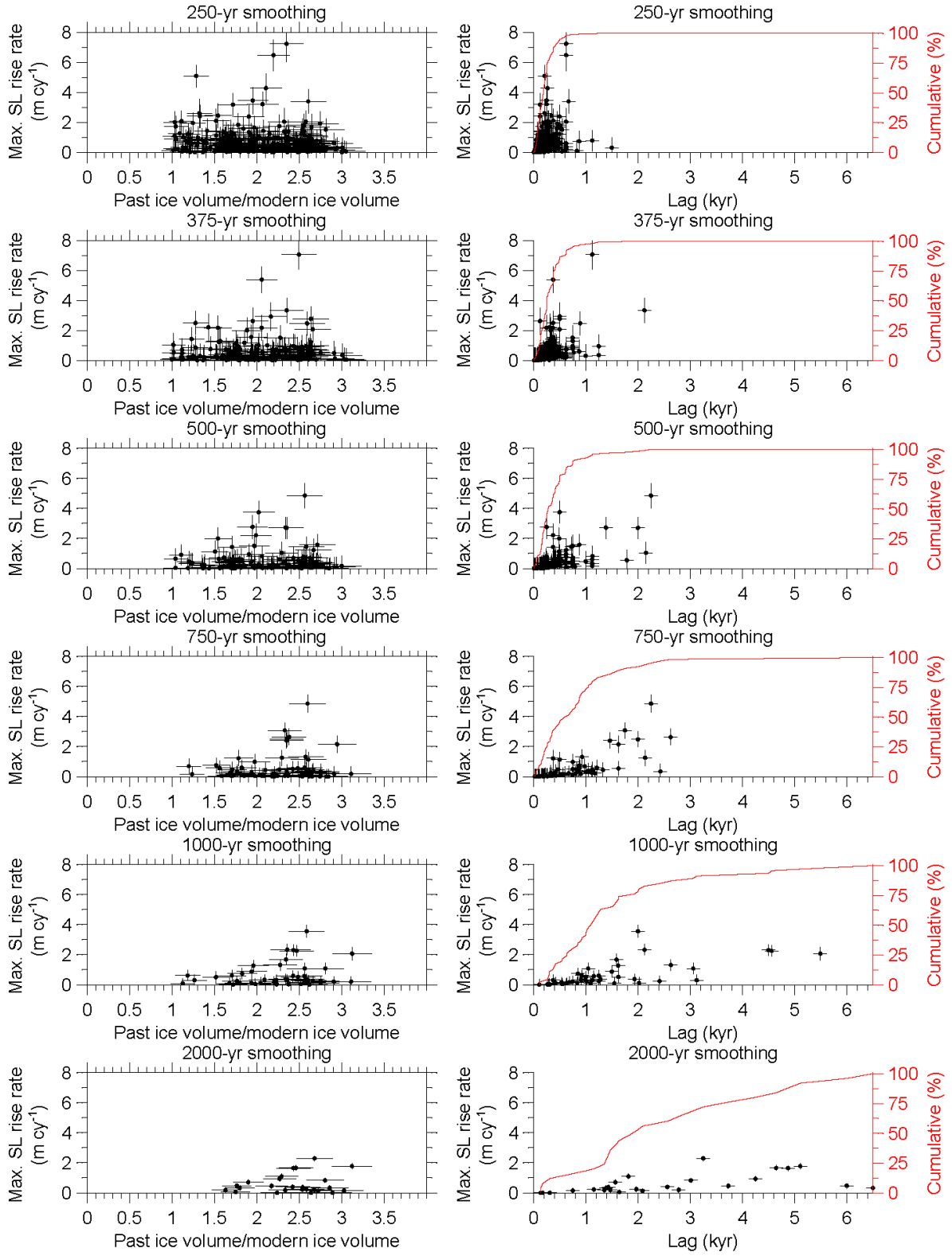

Supplementary Figure 17 Comparison of the effects of different smoothings on our analyses of deglaciation 'pulses'. Maximum sea-level rise rates are plotted against: (**left**) relative ice volume at the start of a deglaciation pulse, and (**right**) lag between the onset of deglaciation pulses and peak sea-level rise rates. The cumulative distribution (red line) of the number of deglaciation pulses as a function of lag is also shown (**right**).

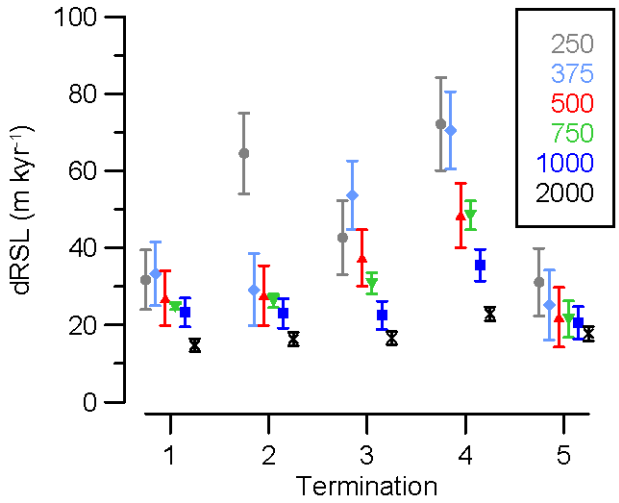

Supplementary Figure 18 The effect of different smoothings (250, 375, 500, 750, 1000 and 2000 year) on maximum sea-level rise rates (dRSL) at glacial terminations 1-5.

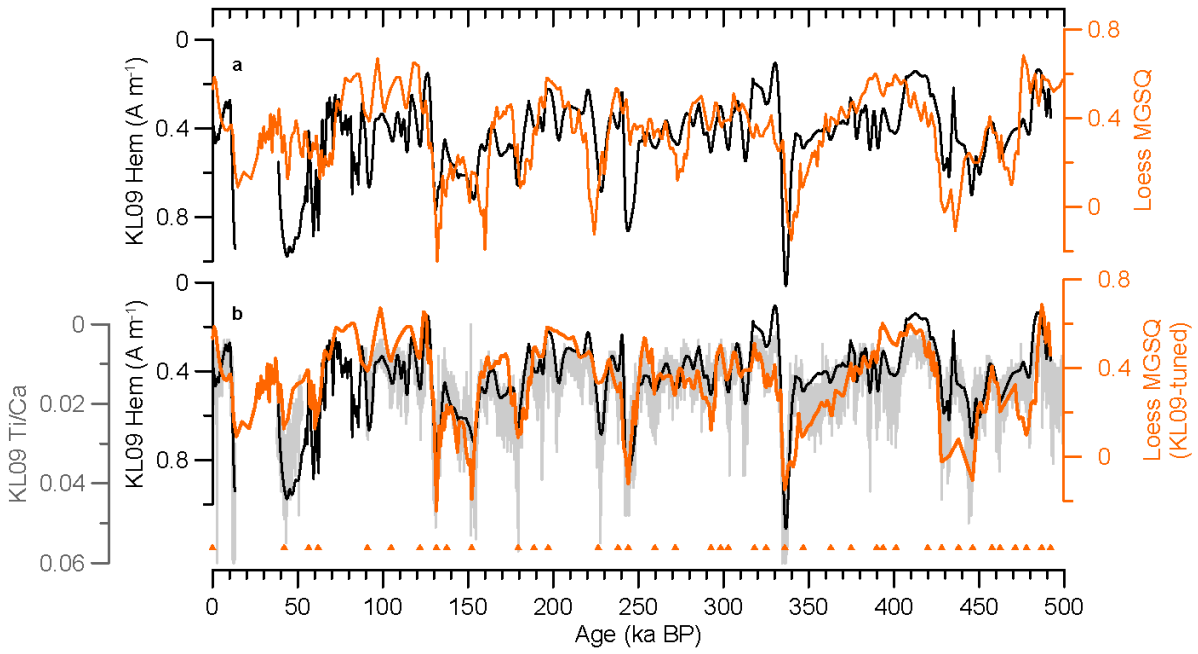

Supplementary Figure 19 Synchronisation of Chinese loess and Red Sea dust records. Red Sea core KL09 Hem (black) and Ti/Ca (grey) records, and the stacked 'mean quartz grain size' (MGSQ) record (orange) on (**a**) its original chronology[27], and (**b**) after correlation with the Red Sea dust record. Correlation ties are indicated as orange triangles.

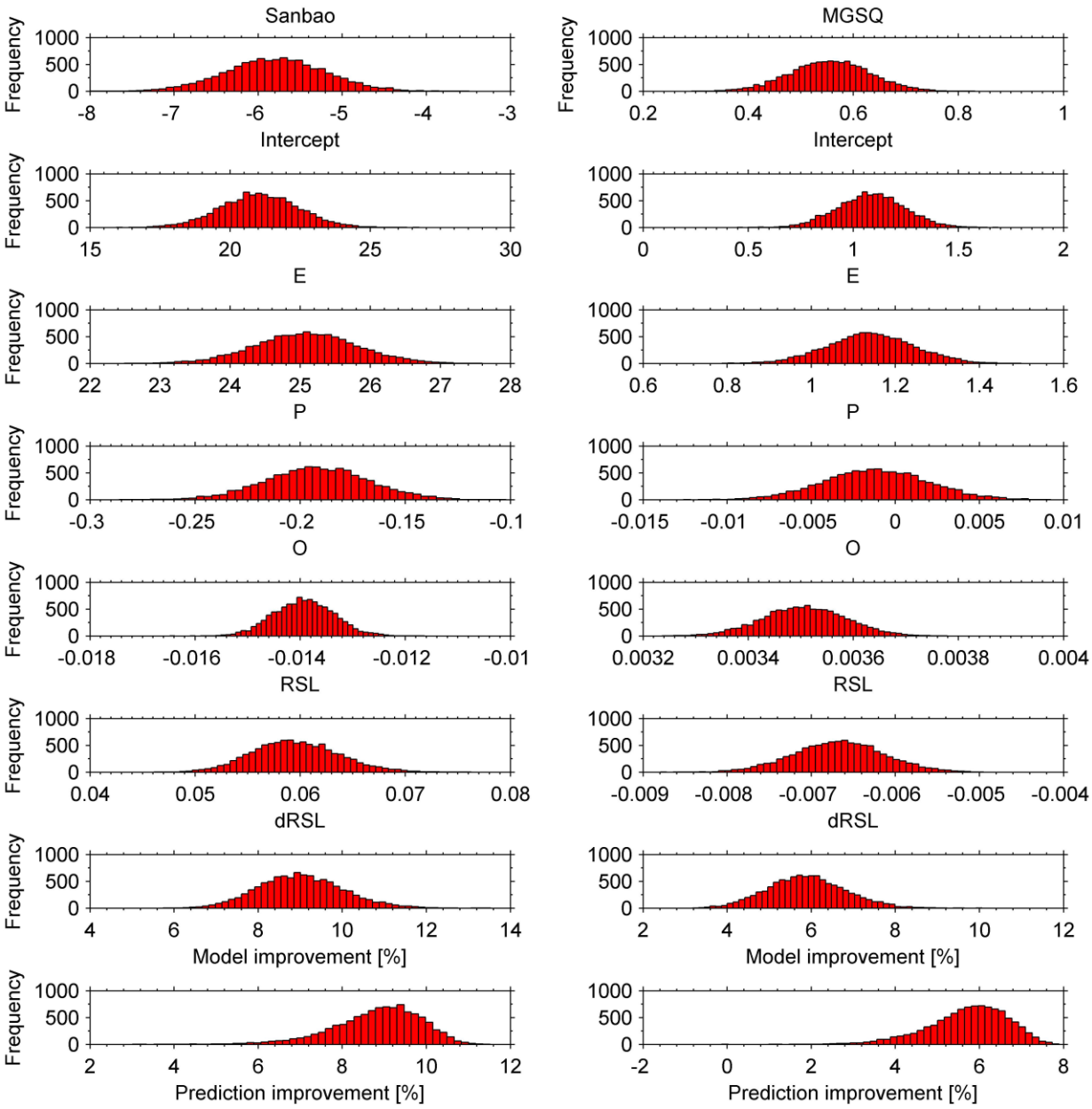

Supplementary Figure 20 Multiple linear regression models (MLRs) for $\delta^{18}O_{sanbao}$ (**left**) and MGSQ (**right**). Frequency distributions are shown for (top to bottom): the intercepts; the coefficients of eccentricity (E), precession (P), obliquity (O), RSL and dRSL; MLR model improvement when the dRSL component is included; MLR model-prediction improvement when the dRSL component is included.

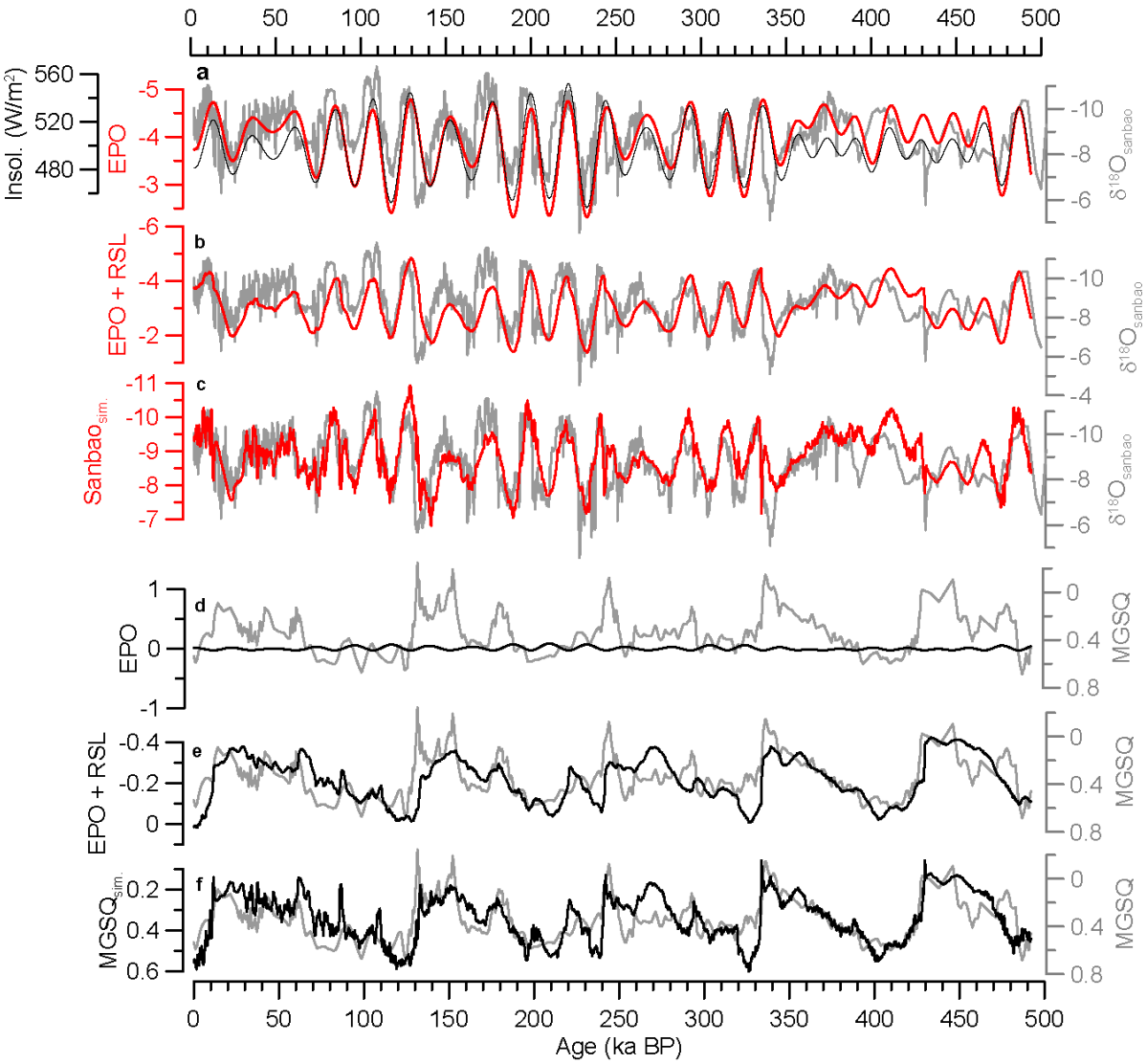

Supplementary Figure 21 Simulations of $\delta^{18}O_{sanbao}$ (**a-c**, red) and MGSQ (**d-f**, black) superimposed on the original $\delta^{18}O_{sanbao}$ and normalised MGSQ time-series (grey). Time-series for the orbital components (EPO; normalised to zero mean and unit variance) and for boreal mid-summer insolation (**a**, black) are from ref. 43. Y-axes in (**a**) and (**d**) are scaled for comparison.

Supplementary Table 1

Tie-points and uncertainties in the dust-$\delta^{18}O_{sanbao}$ and RSL_{dust}-$\delta^{18}O_{sanbao}$ correlations.

Tie_{sanbao} age (kyr)	$Tie_{KL09,RSL}$ age (kyr)	U/Th-dating 2σ (kyr)	$\delta^{18}O_{sanbao}$ sample step (kyr)	KL09 Ti/Ca sample step (kyr)	Peak ID_{Sanbao} 2σ (kyr)	Peak ID_{RSL6} 2σ (kyr)	Phase offset 2σ (kyr)	**RMS 2σ (kyr)**
0.000	0.000	0.000	0.019	0.022				**0.029**
7.875	7.427	0.110			0.032	0.427	1	**1.094**
11.576	11.576	0.696	0.012	0.023				**0.696**
19.824	21.107	1.312			0.062	0.954	1	**1.907**
32.867	35.543	2.828			0.139	1.990	1	**3.602**
43.804	44.794	2.740			0.160	0.795	1	**3.027**
55.015	54.351	1.242			0.128	0.357	1	**1.639**
67.934	65.372	2.976			0.157	0.303	1	**3.158**
80.467	77.013	0.800			0.169	0.395	1	**1.351**
93.136	88.137	1.022			0.096	0.474	1	**1.510**
104.716	99.074	1.192			0.042	0.541	1	**1.648**
115.088	111.121	1.328			0.026	0.663	1	**1.790**
124.761	124.731	0.902			0.022	0.304	1	**1.381**
129.550	129.550	0.710	0.080	0.034				**0.715**
134.734	136.838	1.774			0.024	0.396	1	**2.075**
146.178	147.929	3.238			0.048	0.981	1	**3.528**
160.806	158.269	1.598			0.047	1.128	1	**2.197**
172.672	169.730	2.276			0.028	0.745	1	**2.595**
184.322	183.045	1.798			0.023	1.300	1	**2.434**
195.147	195.743	2.500			0.025	0.663	1	**2.773**
205.808	204.007	2.556			0.043	0.715	1	**2.837**
217.607	211.027	1.670			0.055	0.699	1	**2.069**
229.089	222.561	0.878			0.034	0.649	1	**1.481**
239.359	235.671	0.774			0.030	0.362	1	**1.316**
242.157	242.157	0.472	0.069	0.033				**0.478**
249.501	247.125	0.288			0.046	0.408	1	**1.119**
261.225	257.990	1.052			0.142	0.606	1	**1.579**
276.291	270.260	3.168			0.180	0.858	1	**3.436**
288.593	284.099	3.520			0.152	0.561	1	**3.705**
300.643	295.547	3.230			0.137	0.675	1	**3.451**
310.965	306.586	2.332			0.078	0.964	1	**2.715**
320.401	316.909	0.814			0.039	0.525	1	**1.393**
329.910	328.233	0.504			0.023	0.263	1	**1.151**
334.367	334.367	0.692	0.057	0.031				**0.695**
339.846	339.497	0.918			0.025	0.268	1	**1.384**
350.259	349.645	0.786			0.055	0.492	1	**1.365**
361.729	357.979	1.696			0.136	0.892	1	**2.166**
391.751	394.563	3.790			0.263	0.533	1	**3.965**
404.069	405.830	2.226			0.357	0.619	1	**2.543**
417.193	415.073	1.834			0.391	0.846	1	**2.288**
425.056	424.134	2.162			0.394	0.723	1	**2.520**
429.000	429.000	2.328	3.000	0.028				**3.797**
433.065	435.328	2.322			0.308	0.771	1	**2.661**
443.339	445.775	2.618			0.291	1.169	1	**3.050**
453.496	455.773	3.732			0.519	1.908	1	**4.340**
462.532	462.477	2.632			0.722	1.947	1	**3.498**
474.139	467.772	2.450			0.376	1.069	1	**2.879**
486.111	479.100	4.644			0.169	0.420	1	**4.772**
492.000	492.000	6.452	5.000	0.024				**8.163**

See notes overpage.

(Supplementary Table 1 continued)

Tie-points are based on the $\delta^{18}O_{sanbao}$[ref.7,15], KL09 Ti/Ca[ref.4], and Red Sea RSL[ref.3] chronologies (columns 1-2). Sources of our propagated uncertainties include U/Th-dating of Sanbao Cave stalagmites (column 3), sample-spacing in the $\delta^{18}O_{sanbao}$ and KL09 Ti/Ca records (columns 4-5), peak detection in the filtered $\delta^{18}O_{sanbao}$ and $RSL_{dust\text{-}sanbao}$ records (columns 6-7), and phasing between precession-band covariance in $\delta^{18}O_{sanbao}$ and $RSL_{dust\text{-}sanbao}$ (column 8). Details of how we derived these uncertainties are provided in the main text. A root mean square (RMS) calculation is used to combine the above uncertainties (column 9). Red text denotes data relating to the dust-$\delta^{18}O_{sanbao}$ synchronisation.

Supplementary Table 2
Timing of sea-level highstands prior to the last interglacial (MIS 5e).

	Stage	MIS 7		MIS 9	MIS 11
	Sub-stage	7a	7e	9e	
		(kyr)	(kyr)	(kyr)	(kyr)
RSL ≥0 m	$\mathbf{2\sigma_{pmax}}$	-	-	-	-
	$2\sigma_{data}$	195.4-200.6	239.4-240.1	327.5-334.1	401.1-408.6
RSL ≥-10 m	$\mathbf{2\sigma_{pmax}}$	**196.8-197.4**	**239.4-239.9**	**327.0-331.1**	**401.6-408.8**
	$2\sigma_{data}$	194.1-203.0	238.1-241.3	324.6-334.5	398.1-417.5
RSL ≥-20 m	$\mathbf{2\sigma_{pmax}}$	**195.3-199.5**	**238.4-240.9**	**325.1-333.4**	**398.9-417.6**
	$2\sigma_{data}$	192.9-206.5	236.8-241.9	322.9-334.9	395.5-422.1

RSL values are given for the 95% confidence interval of the maximum-probability sea level ($\mathbf{2\sigma_{pmax}}$), and for the 95% probability interval of all RSL data points ($2\sigma_{data}$).

Supplementary Table 3
Chronologic constraints (lower and upper age boundary) for sea-level rises associated with aggradational units of the Palaeo-Tiber River.

Aggradational Unit (=sea-level rise)	Age boundaries (kyr)
VG	l: 530±2
	u: 488±2
SP	l: 437±8
	u: 410±2
AU	l: <365±4
	u: na
VM	l: na
	u: 285±2
VI	l: 268±5
	u: <253±8

All ages are reported with 2σ uncertainties.

Supplementary Table 4
Summary of lags between the onset of melting episodes and peak sea-level rise rates over the last 500 kyr, calculated for deglaciation events (black text) and pulses (red text), and for different smoothing functions. Results for the 500-yr smoothing (bold) are deemed to be the most useful (see main text).

		Lag (kyr)									
	Smoothing:	*250-yr*		*375-yr*		***500-yr***		*750-yr*		*1000-yr*	
Cumulative number of deglaciation events/pulses:	68%	0.3	0.2	0.6	0.4	**0.6**	**0.4**	1.2	0.9	2.4	1.6
	85%	0.7	0.4	1.5	0.5	**1.5**	**0.6**	3.0	1.4	6.0	2.4
	95%	2.4	0.5	5.0	0.7	**4.5**	**1.1**	7.5	2.2	9.4	4.5

Supplementary Table 5
Tie-points and uncertainties in the MGSQ-KL09 Ti/Ca correlation.

TieKL09 age (kyr)	TieMGSQ age (kyr)	KL09-dating 2σ (kyr)	KL09 Ti/Ca sample step (kyr)	MGSQ sample step (kyr)	RMS 2σ (kyr)
0	0	0	0.030	0.066	0.073
42.081	44.270	2.704	0.030	0.318	2.723
56.385	49.190	2.021	0.030	0.471	2.075
61.988	70.120	3.105	0.030	0.540	3.152
90.930	91.880	2.189	0.030	0.667	2.288
104.860	101.100	1.433	0.030	0.845	1.664
121.830	114.100	1.937	0.030	0.554	2.014
131.439	131.900	1.585	0.030	0.257	1.606
137.506	144.100	2.447	0.030	0.662	2.536
152.151	159.900	3.401	0.030	0.936	3.527
179.398	180.600	2.682	0.030	1.855	3.261
188.721	192.700	2.661	0.030	1.080	2.872
197.063	196.300	2.480	0.030	1.073	2.702
226.385	211.800	2.196	0.030	1.739	2.801
238.080	217.700	1.389	0.030	1.647	2.155
244.080	224.100	1.921	0.030	0.593	2.010
259.656	245.500	1.946	0.030	0.768	2.093
271.627	254.200	3.236	0.030	0.862	3.349
292.614	272.900	3.166	0.030	0.693	3.241
298.257	286.800	2.910	0.030	0.403	2.938
302.760	292.400	2.805	0.030	0.779	2.911
318.174	305.900	1.964	0.030	0.514	2.030
324.972	317.800	2.102	0.030	0.649	2.200
335.916	339.800	1.593	0.030	0.985	1.873
346.761	346.700	2.366	0.030	1.627	2.871
362.927	354.800	2.358	0.030	1.686	2.899
374.847	360.000	4.223	0.030	1.396	4.448
389.947	378.100	3.534	0.030	0.198	3.540
393.605	389.800	3.018	0.030	0.423	3.048
401.244	393.700	2.931	0.030	0.506	2.974
419.848	410.000	2.308	0.030	0.426	2.348
428.064	429.600	1.712	0.030	5.316	5.585
437.946	433.500	2.536	0.030	13.560	13.795
446.185	436.000	2.661	0.030	9.753	10.109
457.565	456.300	2.931	0.030	1.312	3.211
462.320	462.000	2.505	0.030	9.657	9.977
471.226	463.000	2.698	0.030	9.878	10.240
477.816	469.100	3.105	0.030	0.349	3.125
486.721	475.800	3.494	0.030	0.190	3.500
491.994	485.000	4.077	0.030	0.287	4.087

Tie-points are based on the stacked mean quartz grain-size (MGSQ) record[27] on its original chronology, and on the KL09 Ti/Ca record on its new, $\delta^{18}O_{sanbao}$-tuned chronology (this study) (columns 1-2). Sources of our propagated uncertainties include the new KL09 chronology (column 3) and sample-spacing in the KL09 Ti/Ca and MGSQ records (columns 4-5). KL09 dating uncertainties (column 3) were interpolated using OxCal. A root mean square (RMS) calculation is used to combine the above uncertainties (column 6).

Supplementary Table 6
Statistical variance for each component in our MLR models for $\delta^{18}O_{sanbao}$ ($Sanbao_{sim}$) and MGSQ ($MGSQ_{sim}$).

	$Sanbao_{sim}$		**$MGSQ_{sim}$**	
	Mean	±2σ	Mean	±2σ
	(%)		(%)	
Signal variance explained by whole model	36.3	1.2	43.9	1.2
Signal variance explained by E	3.6	0.4	0.6	0.2
Signal variance explained by P	16.0	1.0	2.0	0.3
Signal variance explained by O	1.0	0.3	0.0	0.0
Signal variance explained by RSL	10.0	0.8	37.1	1.2
Signal variance explained by dRSL	5.8	0.6	4.3	0.7

Values denote the mean variance and its standard error (±2σ) for all simulations.

Supplementary Table 7
Summary of cross-spectral phase analyses between $\delta^{18}O_{sanbao}$ and convolutions of our '$Sanbao_{sim}$' record.

	Coh. (%)	Periodicity (kyr)	Phase ±2σ (°)	(kyr)
EPO	94	22.7	39.8±4.8	2.5±0.3
EPO + RSL	93	22.7	33.5±5.2	2.1±0.3
$Sanbao_{sim}$ (EPO + RSL – dRSL)	95	21.7	22.6±4.5	1.4±0.3

See supplementary text for the regression coefficients of the components of $Sanbao_{sim}$. Phases are shown for peak coherencies ('Coh.') between $\delta^{18}O_{sanabo}$ and the convolved records at periodicities equivalent to the precession cycle.

Supplementary Note 1

Correlation of Red Sea dust and RSL to Sanbao Cave $\delta^{18}O$

A recent study provided a tightly-constrained, U/Th-based chronology for a continuous relative sea-level (RSL) record over the past 150 kyr[ref.1]. It exploits a common "glacial effect" among the Mediterranean and Red Seas to develop a correlation between the Red Sea RSL record and Soreq Cave (Israel) speleothem $\delta^{18}O$ variations[1]. This approach cannot be used to date Red Sea RSL variations over the preceding glacial cycles (back to ~500 kyr, see Rohling et al.[ref.2,3]) because the Soreq $\delta^{18}O$ record does not extend beyond ~180 kyr. Here we exploit monsoon-process links between Arabia and East Asia, and a 500-kyr speleothem $\delta^{18}O$ record from Sanbao Cave, China, to provide U/Th-based age control to the Red Sea RSL record between 150 and 500 kyr. This "Sanbao method" is different to that employed in the previously published RSL-Soreq correlation. While it does not reach the same level of age control as the previous method, it offers greatly improved accuracy and chronological advantages for time intervals before 150 kyr compared to existing methods.

Overall, the Sanbao method relies on two synchronisations. The first, between core KL09 Ti/Ca and Sanbao Cave speleothem $\delta^{18}O$ ($\delta^{18}O_{sanbao}$), results in '$RSL_{dust\text{-}sanbao}$'. Thus, the Red Sea RSL record is indirectly synchronised at each glacial termination to $\delta^{18}O_{sanbao}$ based on the Red Sea dust record of Roberts et al.[ref.4]. The second synchronisation, between '$RSL_{dust\text{-}sanbao}$' and $\delta^{18}O_{sanbao}$, results in 'RSL_{sanbao}'. In this case, the first (indirect) RSL synchronisation to $\delta^{18}O_{sanbao}$ is 'fine-tuned' by directly correlating filtered orbital periods in $RSL_{dust\text{-}sanbao}$ and $\delta^{18}O_{sanbao}$ that are common to both records and are directly in phase (within uncertainties).

To correlate Red Sea dust and $\delta^{18}O_{sanbao}$, we use the high-resolution Ti/Ca record of central Red Sea sediment core KL09[ref.4]. This record has a 0.5-mm down-core sampling interval, compared to a 1-cm sampling interval for the environmental magnetic KL09 hematite (Hem) record, which is smoothed by a 4-cm moving Gaussian window due to the width of the magnetometer response function[5]. We correlate mid-points of the rapid decreases in $\delta^{18}O_{sanbao}$ and KL09 Ti/Ca that follow their respective maxima at terminations (main-text Fig. 1b). Use of these mid-points minimises chronological uncertainties relating to potentially real offsets in the onset and end of the transitions[6]. Mid-transition values correspond to ~-8‰ in $\delta^{18}O_{sanbao}$ and ~0.025 in Ti/Ca. We emphasize that this dust-$\delta^{18}O_{sanbao}$ synchronisation is

based on large-scale atmospheric circulation changes at glacial terminations (see main text). Hence, a comprehensive interpretation of the $\delta^{18}O_{sanbao}$ 'response' is unnecessary. In detail, Chinese cave $\delta^{18}O$ variations are influenced by summer and winter monsoon intensity, as well as by local and regional isotope fractionation[7-10].

For correlation between Red Sea RSL and $\delta^{18}O_{sanbao}$, we use the Red Sea RSL record of Rohling et al.[ref.2,3]. This record is predominantly based on RSL data from central Red Sea core KL09, supplemented with RSL data from nearby cores KL1l and MD92-1017. Key to our study is the known phase relationship between Red Sea dust and sea-level records, based on coupled measurements of the same samples from core KL09. The composite (KL09 + KL11 + MD92-1017) and KL09-only RSL records yield identical timings of sea-level change (Supplementary Fig. 2), so that inclusion of data from other cores in the RSL record does not produce spurious phase offsets between dust and RSL. All correlations were performed using the Analyseries software[11].

Synchronisation of KL09 Ti/Ca (dust) and $\delta^{18}O_{sanbao}$, with straightforward linear interpolation between terminations, yields the 'Ti/$Ca_{dust\text{-}sanbao}$' and '$RSL_{dust\text{-}sanbao}$' records (main-text Fig. 1a-c). Their power spectra, and those for $\delta^{18}O_{sanbao}$, all have peaks at frequencies of 0.042-0.045 kyr^{-1}(~23 kyr periodicity), which is equivalent to the precession cycle (Supplementary Fig. 6a). Spectral peaks are also observed for Ti/$Ca_{dust\text{-}sanbao}$ and $RSL_{dust\text{-}sanbao}$ at frequencies equivalent to eccentricity (~0.01 kyr^{-1}; ~100 kyr periodicity), and for $RSL_{dust\text{-}sanbao}$ at obliquity frequencies (~0.025 kyr^{-1}; ~40 kyr periodicity) (Supplementary Fig. 6a). Cross-spectral phase analyses of Ti/$Ca_{dust\text{-}sanbao}$ and $RSL_{dust\text{-}sanbao}$ with $\delta^{18}O_{sanbao}$ reveal strong covariance at frequencies of 0.045 kyr^{-1} (~22 kyr periodicity). Coherency is 78% for Ti/$Ca_{dust\text{-}sanbao}$ and $\delta^{18}O_{sanbao}$, and 90% for $RSL_{dust\text{-}sanbao}$ and $\delta^{18}O_{sanbao}$.

Age uncertainties associated with the $\delta^{18}O_{sanbao}$ chronology are derived from a Bayesian model in the software 'OxCal'[ref.12,13]. Because we wish to maintain consistency with the existing, linearly interpolated $\delta^{18}O_{sanbao}$ chronology[7,14,15], we use the U/Th datings and linearly interpolated ages ('mean estimates') from those studies, and take the estimate of variance from the Bayesian model. Supplementary Figure 8 shows that there is no significant difference in the mean estimates (original versus modelled), hence this approach is justified.

Supplementary Note 2

The Palaeo-Tiber River record

Sea-level forcing on the stratigraphic record.

Several studies (see refs. 16-17, and references therein) have shown that sea-level forcing controlled deposition of sedimentary sections in the coastal plains of the Palaeo-Tiber River and in the alluvial plains of its tributaries near Rome, Italy (Supplementary Fig. 3). Using palaeomagnetic constraints and $^{40}Ar/^{39}Ar$-dated tephra layers intercalated with the sedimentary deposits, these studies demonstrate that the sedimentary sections were deposited during sea-level rise and associated marine ingressions during glacial terminations. The stratigraphic record of each complete, glacially forced sea-level oscillation in a coastal area is represented by a basal erosive surface, which was progressively excavated as a consequence of coastline retreat and sea-level lowering during glacial periods, overlain by a grading upward succession of clastic sediments, rapidly deposited during sea-level rise in response to deglaciation. Generally, the aggradational sections recognised in the coastal area around Rome are fining-upward sequences, with coarse-grained gravel and sand (≤10 m thick) at the base of each section. The basal coarse-grained deposits are followed by relatively thin sand horizons, which grade upward into several metres of silt and clay (Supplementary Fig. 4).

Radiometric age constraints on the sedimentary record deposited within the valley and in the coastal plain of the modern Tiber River[17,18]demonstrate that gravel aggradation marks a unique time span in the depositional history of the river between the end of the Last Glacial Maximum (~21 kyr) and the last glacial termination (~14 kyr). Transportation by the Tiber River of gravel consisting of > 5 cm diameter pebbles required exceptional hydrologic conditions that were not repeated during Holocene time. These conditions, which are characteristic of glacial terminations, include: i) increased sediment supply to the Tiber drainage basin caused by rapid melting of the Apennine glaciers and subsequent release of a large amount of clastic material; and ii) lower sea level that produces a steeper baseline gradient and thus greater erosive competence of the Tiber River. These conditions would have worked in concert during the 21-14 kyr interval, until accelerated sea-level rise led to a rapid drop in competence of the Tiber River and, consequently, to the start of sandy clay deposition. Based on the modern Tiber River analogue, this principle has been applied to interpret older, exposed aggradational successions (Supplementary Fig. 4). Ages of the primary volcanic layers intercalated within the clayey deposits above the basal gravel

sections were then used to constrain the timing of the associated sea-level rise (Supplementary Fig. 5, Supplementary Table 3).

Chronostratigraphy.

$^{40}Ar/^{39}Ar$ datings used to constrain the timing of sea-level rises (Supplementary Fig. 3) were performed at the Berkeley Geochronology Center using procedures and facilities described by Karner and Renne[ref.19]. All $^{40}Ar/^{39}Ar$ ages published by Karner and Renne [ref.19] that adopted the age of 27.84 Ma for the Fish Canyon sanidine standard[20] have been re-calculated according to the standard age of 28.02 ± 0.16 Ma[ref.21], in order to harmonise them with published datings[16,22]. While two recent revisions of the Fish Canyon sanidine age have been proposed[23,24], their reliability has been questioned[25] based on the fact that, if adopted, they would shift the the $^{40}Ar/^{39}Ar$ age of the Matuyama-Brunhes reversal to 781 ka and 784 ka, respectively. These ages conflict with astrochronological estimates. According to Channell et al.[ref.25] , using the recently revised, older ages for the standard systematically increases the offset between the timing for glacial terminations inferred from the sedimentary record of the Palaeo-Tiber River and that provided by astrochronological calibration (e.g., ref. 26). We therefore adopt a conservative approach and use the age of 28.02 Ma for the standard to calibrate ages presented here. Regardless, the disputed $^{40}Ar/^{39}Ar$ ages are well outside the time interval of our sea-level record, hence they do not apply to our age-model validation.

Supplementary Note 3

Correlation between Chinese loess and Red Sea dust records

Striking similarity between KL09 Hem and a stacked mean quartz grain-size record (MGSQ[ref.27]) from the Chinese Loess Plateau[4] reflects a broadly synchronous response to atmospheric changes within the wider monsoon region (Supplementary Fig. 19a). Although the dynamic processes that link these records have not yet been explored in detail, their obvious visual similarity and association with monsoonal atmospheric circulation (see main text) strongly suggest that they can be synchronised. We therefore correlate MGSQ with the Red Sea dust records (KL09 Ti/Ca and Hem) on their new, $\delta^{18}O_{sanbao}$-tuned chronology, using both dust records for tie-point guidance: the Hem and MGSQ records appear more similar in structure because they are of comparable resolution, but the higher-resolution Ti/Ca record more accurately determines tie-point ages (Supplementary Fig. 19b). Note that there are two potential dust ‘spikes’ to which the MGSQ record at 225 ka (on the Sun et al.[ref.27]chronology)

may be aligned: at 230 ka, and at termination 4 (245 ka). Given that *i)* the largest excursions in the KL09 dust records are at glacial terminations, *ii)* the most dramatic negative excursions in MGSQ (indicative of stronger winter monsoons) generally coincide with Red Sea dust spikes at terminations, *iii)* stronger Asian winter monsoons are associated with glacial terminations, and *iv)* there is a known process link between large-scale atmospheric circulation over Arabia and East Asia, it is reasonable to assume that the negative MGSQ excursion at 225 ka (Supplementary Fig. 17a) should be aligned with the Red Sea dust spike at 245 ka (termination 4) rather than that at 230 ka Supplementary Fig. 19b). We know that this dust spike is associated with a glacial termination because the Red Sea dust and sea-level records were measured on the same sample suite. Fully-propagated tie-point uncertainties are given in Supplementary Table 5.

The significant advantages of this exercise are a common timescale for past ice-volume variability and Asian winter monsoon (AWM) intensity, and a U/Th-based chronology for MGSQ. The latter was previously dated[27] by correlation with orbital precession and obliquity assuming *i)* zero phase lag between a $\delta^{18}O$ ice-volume proxy ("SPECMAP"[ref.28]) and AWM maxima, and *ii)* 8-kyr and 5-kyr ice-volume phase lags relative to obliquity and precession, respectively[28]. Our dust-MGSQ correlation therefore allows MGSQ to be dated, and ice-volume and AWM records to be synchronised, without assumptions about ice-volume phasings and unbiased by uncertainties associated with the SPECMAP $\delta^{18}O$ record.

Supplementary references

1. Grant, K.M. *et al.*, Rapid coupling between ice volume and polar temperature over the past 150,000 years. *Nature* **491**, 744-747 (2012).
2. Rohling, E.J. *et al.*, Antarctic temperature and global sea level closely coupled over the past five glacial cycles. *Nature Geosci.* **2**, 500-504 (2009).
3. Rohling, E.J. *et al.*, Comparison between Holocene and Marine Isotope Stage-11 sea-level histories. *Earth Planet. Sci. Lett.* **291**, 97-105 (2010).
4. Roberts, A.P., Rohling, E.J., Grant, K.M., Larrasoaña, J.C., Liu, Q., Atmospheric dust variability from Arabia and China over the last 500,000 years. *Quat. Sci. Rev.* **30**, 3537-3541 (2011).
5. Roberts, A.P., High-resolution magnetic analysis of sediment cores: strengths, limitations and strategies for maximizing the value of long-core magnetic data. *Phys. Earth Planet. Inter.* **156**, 162-178 (2006).
6. Shackleton, N.J., The 100,000-year ice-age cycle identified and found to lag temperature, carbon dioxide, and orbital eccentricity. *Science* **289**, 1897-1902 (2000).
7. Cheng, H. *et al.*, Ice age terminations. *Science* **326**, 248-252 (2009).
8. Clemens, S.C., Prell, W.L., & Sun, Y., Orbital-scale timing and mechanisms driving Late Pleistocene Indo-Asian summer monsoons: Reinterpreting cave speleothem $\delta^{18}O$. *Paleoceanography* **25**, PA4207 (2010).
9. Lewis, S.C., LeGrande, A.N., Kelley, M., & Schmidt, G.A., Water vapour source impacts on oxygen isotope variability in tropical precipitation during Heinrich events. *Clim. Past* **6**, 325-343 (2010).
10. Pausata, S.F.R., Battisti, D.S., Kerim, H., Nisancioglu, K.H., & Bitz, C.M., Chinese stalagmite $\delta^{18}O$ controlled by changes in the Indian monsoon during a simulated Heinrich event. *Nat. Geosci.* **4**, 474-480 (2011).
11. Paillard, D., Macintosh Program performs time-series analysis. *Eos Trans. Am. Geophys. Union* **77**, 39 (1996).
12. Bronk Ramsey, C., Deposition models for chronological records. *Quat. Sci. Rev.* **27**, 42-60 (2008).
13. Bronk Ramsey, C., Bayesian analysis of radiocarbon dates. *Radiocarbon* **511**, 337-360 (2009).
14. Wang, Y.J. *et al.*, Millennial- and orbital-scale changes in the East Asian monsoon over the past 224,000 years. *Nature* **451**, 1090-1093 (2008).
15. Cheng, H. *et al.*, The climatic cyclicity in semiarid-arid central Asia over the past 500,000 years. *Geophys. Res. Lett.* **39**, L01705 (2012).
16. Florindo, F. *et al.*, Radioisotopic age constraints for Glacial Terminations IX and VII from aggradational sections of the Tiber River delta in Rome, Italy. *Earth Planet. Sci. Lett.* **256**, 61-80 (2007).
17. Marra, F., Florindo, F., Boschi E., The history of glacial terminations from the Tiber River (Rome): insights to glacial forcing mechanisms. *Palaeoceanography* **23**, PA2205 (2008).
18. Marra, F., Bozzano, F., Cinti, F.R., Chronostratigraphic and lithologic features of the Tiber River sediments (Rome, Italy): implications on the post-glacial sea-level rise and Holocene climate. *Global Planet. Change* **107**, 157-176 (2013).
19. Karner, D.B., Renne, P.R., $^{40}Ar/^{39}Ar$ geochronology of Roman province tephra in the Tiber River Valley: age calibration of Middle Pleistocene sea-level changes. *Geol. Soc. Am. Bull.* **110**, 740-747 (1998).

20. Renne, P.R., Excess ^{40}Ar in biotite and hornblende from the Noril'sk 1 Intrusion, Siberia; implications for the age of the Siberian Traps. *Earth Planet. Sci. Lett.* **131**, 165-176 (1995).
21. Renne, P.R. *et al.*, Intercalibration of standards, absolute ages and uncertainties in ^{40}Ar/^{39}Ar dating. *Chem. Geol.* **145**, 117-152 (1998).
22. Karner, D.B., Marra, F., Renne, P.R., The history of the Monti Sabatini and Alban Hills volcanoes: groundwork for assessing volcanic-tectonic hazards for Rome. *J. Volc. Geotherm. Res.* **107**, 185-215 (2001).
23. Kuiper, K.F. *et al.*, Synchronizing rock clocks of Earth history. *Science* **320**, 500-504 (2008).
24. Renne, P.R., Mundil, R., Balco, G., Min, K., Ludwig, K.R., Joint determination of ^{40}K decay constants and ^{40}Ar*/^{40}K for the Fish Canyon sanidine standard, and improved accuracy for ^{40}Ar/^{39}Ar geochronology. *Geochim. Cosmochim. Acta* **74**, 5349-5367 (2010).
25. Channell, J.E.T., Hodell, D.A., Singer, B.S., Xuan, C., Reconciling astrochronological and ^{40}Ar/^{39}Ar ages for the Matuyama-Brunhes boundary and late Matuyama chron. *Geochem. Geophys. Geosyst.* **11**, Q0AA12 (2010).
26. Lisiecki, L.E., Raymo, M.E., A Pliocene-Pleistocene stack of 57 globally distributed benthic δ^{18}O records. *Palaeoceanography* **20**, PA1003 (2005).
27. Sun., Y., Clemens, S.C., An, Z., & Yu, Z., Astronomical timescale and palaeoclimatic implication of stacked 3.6-Myr monsoon records from the Chinese Loess Plateau. *Quat. Sci. Rev.* **25**, 33-48 (2006).
28. Imbrie, J. *et al.*, The orbital theory of Pleistocene climate: support from a revised chronology of the marine δ^{18}O record. In *Milankovitch and Climate (Part I)*, A. Berger *et al.*, Eds. (Reidel, Hingham, Mass., 1994) pp. 269-305.
29. Karner, D.B., Marra, F., Florindo, F., Boschi, E., Pulsed uplift estimated from terrace elevations in the coast of Rome: evidence for a new phase of volcanic activity? *Earth Planet. Sci. Lett.* **188**, 135-148 (2001).
30. Marra, F., Karner, D.B., Freda, C., Gaeta, M., Renne, P., Large mafic eruptions at Alban Hills Volcanic District (Central Italy): Chronostratigraphy, petrography and eruptive behavior, *J. Volc. Geotherm. Res.* **179**, 217-232 (2009).
31. Marra, F., Rosa, C., Stratigrafia e assetto geologico dell'area romana, in "La Geologia di Roma. Il Centro Storico", *Mem. Descr. Carta Geol. Ital.* **50**, 49-118 (1995)
32. Karner, D.B., Marra, F., Correlation of fluviodeltaic aggradational sections with glacial climate history: a revision of the classical Pleistocene stratigraphy of Rome. *Geol. Soc. Am. Bull.* **110**, 748-758 (1998).
33. Marra, F., Florindo, F., Karner, D.B., Palaeomagnetism and geochronology of early Middle Pleistocene depositional sequences near Rome: comparison with the deep sea δ^{18}O climate record. *Earth Planet. Sci. Lett.* **159**, 147-164 (1998).
34. Marra, F., Commento a: Giordano, G., Esposito, A., De Rita, D., Fabbri, M., Mazzini, I., Trigar,i A., Rosa, C., Funiciello, R., 2003 - The sedimentation along the roman coast between middle and upper Pleistocene: the interplay of eustatism, tectonics and volcanism – new data and review, Il Quaternario, 16, 121-129. *Il Quaternario* **17**, 643-645 (2004).
35. Muhs, D.R., Pandolfi, J.M., Simmons, K.R., Schumann, R.R., Sea-level history of past interglacial periods from uranium-series dating of corals, Curaçao, Leeward Antilles islands. *Quat. Res.* **78**, 157-169 (2012).
36. Andersen, M.B. *et al.*, The timing of sea-level high-stands during Marine Isotope Stages 7.5 and 9: constraints from the uranium-series dating of fossil corals from Henderson Island. *Geochim. Cosmochim. Acta* **74**, 3598-3620 (2010).

37. Stirling, C.H. *et al.*, Orbital forcing of the marine isotope stage 9 interglacial. *Science* **91**, 290-293 (2001).
38. Schellmann, G., Radtke, U., A revised morpho- and chronostratigraphy of the Late and Middle Pleistocene coral reef terraces on Southern Barbados (West Indies). *Earth Sci. Rev.* **64**, 157-187 (2004).
39. Hearty, P.J., Kindler, P., Cheng, H., Edwards, R.L., A +20 m middle Pleistocene sea-level highstand (Bermuda and the Bahamas) due to partial collapse of Antarctic ice. *Geology* **27**, 375-378 (1999).
40. Murray-Wallace, C.V., Pleistocene coastal stratigraphy, sea-level highstands and neotectonism of the southern Australian passive continental margin – a review. *J. Quat. Sci.* **17**, 469-489 (2002).
41. Bard, E., Antonioli, F., Silenzi, S., Sea-level during the penultimate interglacial period based on a submerged stalagmite from Argentarola Cave (Italy). *Earth Planet. Sci. Lett.* **196**, 135-146 (2002).
42. Dutton, A. *et al.*, Phasing and amplitude of sea-level and climate change during the penultimate interglacial. *Nature Geosci.* **2**, 355-359 (2009).
43. Laskar, J., The chaotic motion of the solar system: A numerical estimate of the size of the chaotic zones. *Icarus* **88**, 266-291 (1990).